



Original Article

Modification of high-entropy alloy AlCoCrFeNi by electron beam treatment



Victor Gromov ^a, Yurii Ivanov ^{a,b}, Sergey Konovalov ^{a,c,*}, Kirill Osintsev ^{a,c}, Alexander Semin ^a, Yulia Rubannikova ^a

^a Siberian State Industrial University, Novokuznetsk, 654007, Russia

^b Institute of High Current Electronics of the Siberian Branch of the RAS, Tomsk, 634055, Russia

^c Samara National Research University, Samara, 443086, Russia

ARTICLE INFO

Article history:

Received 21 February 2021

Accepted 9 May 2021

Available online 14 May 2021

Keywords:

High-entropy alloy Al–Co–Cr–Fe–Ni

Wire-arc additive manufacturing

Deformation

Electron-beam processing

Structure

ABSTRACT

In this study, a high-entropy alloy (HEA) of Al–Co–Cr–Fe–Ni system was fabricated via wire-arc additive manufacturing technology (WAAM) in the atmosphere of pure Ar followed by high-intensity electron beam treatment. SEM, TEM, and X-ray diffraction methods were used to characterize the manufactured material's microstructure. The HEA has the following composition: Al (36.5 at. %), Ni (33.7 at. %), Fe (16.4 at. %), Cr (8.6 at. %) and Co (4.9 at. %). The obtained material without electron beam treatment has a polycrystalline structure with a grain size of 4–15 μm . Bulks of grains are enriched in Al and Ni, while grain boundaries contain Cr and Fe. Co is quasi-uniformly distributed in the crystal lattice of the manufactured HEA. The ultimate material strength in testing for compression depends on production mode and varies within the interval from 652 to 1899 MPa. The HEA wear parameter amounts to $1.4 \cdot 10^{-4} \text{ mm}^3/\text{N} \cdot \text{m}$, friction coefficient - 0.65. In testings for tension, the material failure occurred by the mechanism of intragrain cleavage. The formation of brittle cracks along boundaries and in grain boundary junctions, i.e. in sites containing the inclusions of second phases, is revealed. The HEA's irradiation by a pulsed electron beam with the energy density of 10–30 J/cm^2 (pulse duration 200 μs , number of pulses 3) results in material homogenization, decreased crystal lattice microdistortions, and an increase in sizes of coherent scattering regions. High-velocity crystallization of the molten surface layer of HEA samples is accompanied by columnar structure formation having a submicrocrystalline structure.

© 2021 The Author(s). Published by Elsevier B.V. This is an open access article under the CC BY-NC-ND license (<http://creativecommons.org/licenses/by-nc-nd/4.0/>).

1. Introduction

One of the fundamental and practically oriented tasks of solid-state physics and physical materials science is the

development of physical bases of creating new metallurgical materials with a complex of necessary physico-mechanical and functional properties and technologies of their production. As it is known, mechanical properties of materials depend essentially on their chemical composition and

* Corresponding author.

E-mail address: ksev@ssau.ru (S. Konovalov).

<https://doi.org/10.1016/j.jmrt.2021.05.012>

2238-7854/© 2021 The Author(s). Published by Elsevier B.V. This is an open access article under the CC BY-NC-ND license (<http://creativecommons.org/licenses/by-nc-nd/4.0/>).

characteristic features of the structural state, such as type, grain size, the form of their boundaries, quality grade, quantity and distribution in size and volume of excess phases, density and type of dislocation substructure, etc.

Considerable improvement of complex of practical design, functional and technological parameters of alloys and intermetallics was connected with additional micro- and microalloying (with the third, fourth, fifth, sixth elements), development of special strengthening and plastifying technologies of both synthesis and subsequent treatment of poly- and monocrystals, modification of their micro- and submicrocrystalline structures. At the beginning of the 21st century, the publications on creating and complex studying new so-called high-entropy polymetallic alloys including 5–6 or more principal elements appeared.

In scientific articles [1–14], published in 2000–2015 years, studying the methods for obtaining high-entropy alloys (HEA) of different chemical composition, microstructure and properties are considered. It is necessary to add the articles [15–20] in which the effect of thermal and deformation treatment on the structure and mechanical properties of HEA alloys were analyzed. The original results obtained in the field of HEA before 2015 are considered in detail in analytical reviews [20–23] where the HEA thermodynamics is described, results of modelling of their structure are considered and new variants of methods for obtaining the multi-component alloys are discussed.

The HEA studies have shown that it is possible to form nanodimensional structures and even amorphous phases due to considerable distortions of lattice caused by the difference in the atomic radii of substitution elements. In this case, the rate of diffusion processes decreases and, as a result, the speed of crystal growth reduces [24,25].

By now, there is no unambiguous answer to this question. It is connected with the fact that «Direct comparison of data is difficult, due to differences in the type and concentration of principal elements, the type and extent of thermo-mechanical processing, and the temperature and duration of post-process thermal treatment» [26].

Practically all types of such alloys (structural, cryo- and heat resistant, corrosion-resistant, those with unique magnetic and electrical properties), as well as compounds (carbides, nitrides, oxides, borides, silicides), are being developed. In most cases, researchers succeed in obtaining a single-phase high-entropy material or multi-phase material consisting of a multi-component matrix and inclusions, which may result in dispersion hardening [27].

Improvement of alloy properties can be achieved by treating the surface with concentrated energy flows. The main feature of hardening materials with concentrated energy fluxes, compared with traditional thermal and chemical-thermal treatment, is the nanostructure of their surface layers. It means a decrease in the scale level of localization of plastic deformation of the surface, which leads to a more uniform distribution of elastic stresses near it under the influence of operational factors. As a result, the probability of nucleation of microcracks in the surface layer leading to failure is significantly reduced. It increases both strength and ductility.

One of the most promising and highly effective surface hardening methods is electron and ion beam processing [28–33]. Electron beam processing provides ultrahigh heating rates (up to 10^6 K/s) of the surface layer to predetermined temperatures and cooling of the surface layer due to heat removal to the bulk of the material at speeds of 10^4 – 10^9 K/s, resulting in the formation of non-uniform submicron nanocrystalline structural phase states [34].

The purpose of this work is to investigate the structure-phase state and properties of high-entropy alloy AlCoCrFeNi subjected to electron beam treatment.

2. Material and methods of investigation

To form the bulk samples of high-entropy (HEA) of the AlCoCrFeNi system, a multi-component (stranded) wire was used as the initial material. It consisted of three strands of different elemental composition: aluminium wire (Al \approx 99.95%, 0.5 mm in diameter), chromium-nickel wire Cr20Ni80 (Cr \approx 20%, Ni \approx 80%, 0.4 mm in diameter), as well as wire of precision alloy 29NK (Co \approx 17%, Fe \approx 54%, Ni \approx 29%, 0.4 mm in diameter) (Fig. 1b).

The multi-component wire was manufactured by the automated stranding of the given three wires on the original setup. The rotation frequency of receiving coil and feeding coils varied to choose the optimal mode of stranding and provide a successful (without jamming and ruptures) passage of wire in the guiding channel and torch. The diameter of the combined wire manufactured by the method amounted to \approx 1 mm.

Fabrication of HEA samples was done by layer-by-layer deposition on steel substrate by means of wire-arc additive manufacturing (WAAM) (cold metal transfer (CMT)) in the atmosphere of inert gas (Ar \approx 99.99%) (Fig. 1a). The following working parameters of deposition complex were constant: rate of wire feeding – 8 m/min, deposition voltage – 17 V, travel speed – 0.3 m/min, gas supply speed (Ar) – 14 l/min.

Three approaches were used in the formation of HEA samples: 1) deposition of all metal layers “from left to right”, at substrate temperature of 25 °C; 2) deposition of all metal

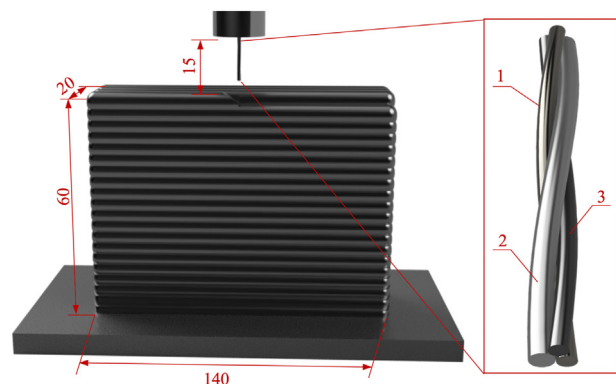


Fig. 1 – Diagram of wire-arc additive manufacturing using a cable consisting of 3 strands and 3D-model of the wire used. 1 – chromium-nickel wire Cr20Ni80, 2 – aluminium wire, 3 – precision alloy wire 29NK.

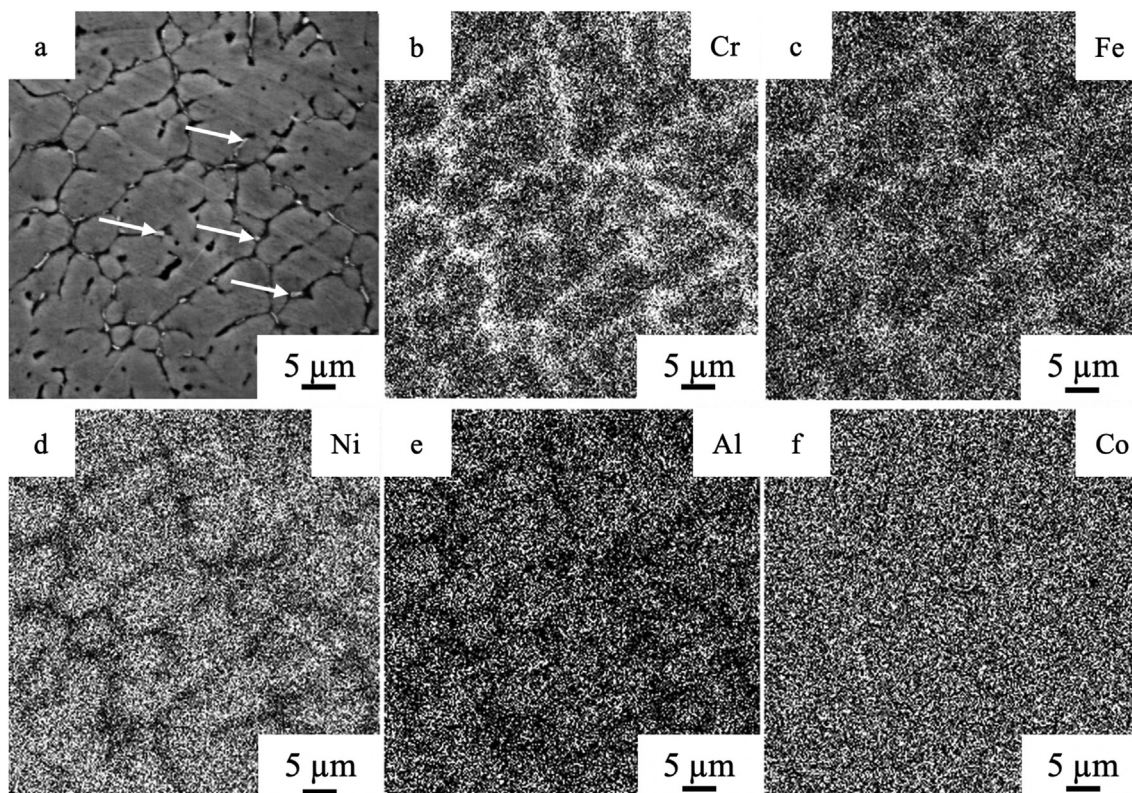


Fig. 2 – SEM (a), of HEA surface and images of the given surface portion obtained in characteristic X-ray radiation of different atoms. The second-phase inclusions are indicated by arrows in a. Scanning electron microscopy.

layers “from left to right” at substrate temperature of 250 °C; 3) deposition of metal from left to right then from right to left” and vice versa, at the substrate temperature of 250 °C.

The resultant HEA samples had sizes of $\approx 60 \times 140 \times 20$ mm and were parallelepipeds consisting of 20 deposited layers in height and 4 layers in thickness. The X-ray fluorescence analysis showed that the manufactured alloy had the following elemental composition (at. %): 28.40 Al, 6.47 Co, 8.36 Cr, 19.57 Fe, 37.20 Ni.

Elemental and phase composition of the alloy, state of the defective substructure were studied by the methods of scanning electron microscopy (microscope “LEO EVO 50”, Carl Zeiss) with energy dispersion analyzer INCA-energy and TESCAN VEGA with energy dispersion analyzer INCAx-act) and transmission electron diffraction microscopy (instrument JEM 2100, JEOL). To reveal the alloy microstructure, the etching of samples preliminary polished on abrasive paper of different grain sizes and abrasive paste by HNO₃ and HCl solution in the ratio of 1:3 was performed. The phase composition and crystal lattice state of main phases of HEA samples were studied by the methods of X-ray phase and X-ray structural analysis (X-ray diffractometer Shimadzu XRD 6000 and DRON-7); the research was done in radiation Cu-K α 1. Phase composition analysis was performed using database PDF 4+ and a program of full-profile analysis POWDER CELL 2.4.

The HEA mechanical properties were characterized by microhardness value being determined on microhardness

tester HV-1000 and nanohardness value (nanotester NanoScan-4D). Measurements were taken both along deposited layers and in a perpendicular, cross-section to detect material homogeneity degrees.

Tribological properties (wear resistance and friction factor) were determined on planar samples using tribometer Pin on Disc and Oscillating TRIBotester (TRIBOtechnic, France) with the following parameters: 6 mm diameter ball made of Al₂O₃ ceramic material, the sample rotation rate of 25 mm/s, the path travelled by counterbody of 100 m, indenter load of 5 N, wear track radius of 2 mm, at room temperature and normal humidity. The degree of material wear was determined by results of track profilometry formed under tests.

Electron-beam processing was performed (device SOLO) with the following parameters: energy of accelerated electrons $U = 18$ keV, energy density of electron beam $ES = (10, 15, 20, 25, 30)$ J/cm², pulse duration of electron beam $f = 200$ μs, pulse number $N = 3$. Irradiation was done in vacuum at pressure of residual gas (argon) $p = 0.02$ Pa in setup chamber.

3. Results and discussion

The images of the HEA sample cross-section's microstructure allowed us to determine that deposited layers had dendritic structures. Dendrites are oriented along heat removal direction. Grain sizes increase as the interface of deposited layers is approached.

A characteristic image of HEA samples' structure obtained by scanning electron microscopy methods is shown in Fig. 2. Surface etching of HEA samples results in revealing the grain structure (Fig. 2, a). Grain sizes vary in the range from 4 μm to 15 μm , which agree with the results obtained by the method of optical microscopy. Along boundaries and in grain volume, the second phase inclusions are revealed (Fig. 2, a, inclusions are indicated by arrows).

The alloy's elemental composition was studied by the method of micro-X-ray spectral analysis (Fig. 3). The material under study contains aluminium, iron, nickel, chromium, and cobalt atoms. The results of the quantitative analysis of the elemental composition of the alloy under study (averaging was carried out over five randomly selected sections) showed that the main elements of the alloy section under study are aluminium (36.5 at. %), nickel (33.7 at. %), iron (16.4 at. %), chrome (8.6 at. %) and cobalt (4.9 at. %). By mapping methods, it is established that near-boundary volumes of the alloy (volumes located along grain boundaries) are enriched in chromium and iron atoms. The grain volume is enriched in nickel and aluminium atoms cobalt is quasi-uniformly distributed in the alloy (Fig. 2, b-f).

The thermogravimetric analysis allowed us to determine the melting temperature of the produced high-entropy alloy. Differential thermal analysis is performed using the instrument for synchronous thermal analysis SetaramLabSys Evo. It is established that the melting temperature of produced high-entropy alloy equals 1495.18 $^{\circ}\text{C}$.

The samples of three regions locating at different distances from the substrate (15 mm, 35 mm, and 55 mm) were prepared to reveal the regularities of structure formation. The samples were studied by the phase analysis from X-ray diffraction patterns. Comparing the obtained X-ray diffraction patterns detected no shift of diffraction peaks and no change in the value of the ratio of diffraction peak intensity to maximum peak intensity. The obtained results are indicative of the phase composition homogeneity of manufactured high-entropy alloy.

Fig. 4 represents the results of diffractogram pattern indexing of HEA under study. It is determined that the sample crystal lattice has a primitive cubic structure with a lattice parameter of 0.288337 nm and a space group of Pm3m. The revealed diffraction maximums may be described in one crystal lattice frameworks, namely, $\text{Fe}_{0.258}\text{Ni}_{1.164}\text{Al}_{0.578}$.

However, it should be taken into account that the results obtained by the methods of scanning electron microscopy

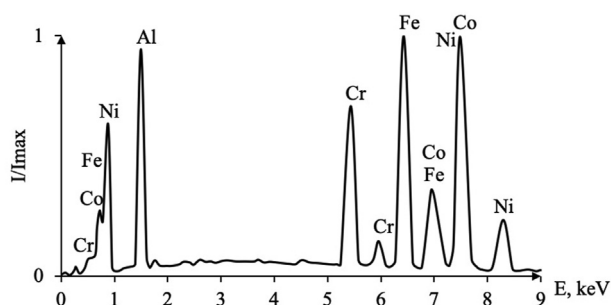


Fig. 3 – Energy spectra of high-entropy alloy.

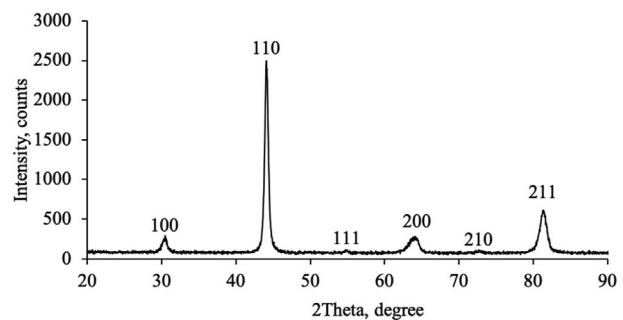


Fig. 4 – X-Ray diffraction pattern portion obtained from HEA sample.

testify to the multi-phase composition of the alloy. The qualitative analysis of the diffraction pattern consisting of the facts enables us to suggest the alloy's following phase composition. The quantitative phase analysis showed the following phases (at. %): 36.56% AlNi, 27.02% CrFe, 36.42% Al_2FeCo .

The alloy's structural analysis by the transmission electron microscopy methods allowed the investigation of the distribution of elemental composition, state of defective substructure, and morphology of material phases at submicro- and nanodimensional levels. It is detected that inclusions of two-dimensional classes: submicron inclusions (Fig. 5, a-c) and nanodimensional inclusions (Fig. 5, d, particles are indicated by arrows) are present in the alloy.

The investigation into the particles' elemental composition revealed in the alloy is performed using micro-X-ray spectral analysis methods (Fig. 6). The results of the quantitative analysis of particles' elemental composition are presented in Table 1.

When analyzing the results presented in Table 1, some amount of oxygen and carbon atoms can be noted in the analyzed portion of foil, along with the specified elements (Al, Fe, Cr, Co, Ni). In this case, the carbon was detected mainly in the bulk of second phase inclusions. Therefore, based on micro-X-ray spectral analysis results, it may be supposed that the inclusions being present on the foil portion are carbides. The main elements of carbides are chromium and iron.

The microhardness analysis by Vickers method at indenter load of 1 N was carried out and it was performed using 5 or more measurements in 14 areas in every 5 mm in sample cross-section. The 4% increase in microhardness value was found in the area located on the boundary with the substrate that may be related to the 10% increase in iron content revealed in the course of layer-by-layer elemental analysis. In the remaining areas, value deviates from the average one by no more than 2%. As a result of performed studies, it is established that the mean microhardness value of the samples produced by mode No. 1 amounts to 474 ± 18 HV, by mode No. 2— 465 ± 3 HV, by mode No. 3— 474 ± 8 HV.

Rockwell hardness measurement by indentation of the diamond tip with a load of 1500 N depending on the substrate's distance showed growth of hardness value in the area adjacent to the substrate. The hardness amounted to 9% compared to the mean value. The Rockwell hardness measured in 3 areas located at distances of 50 mm, 30 mm,

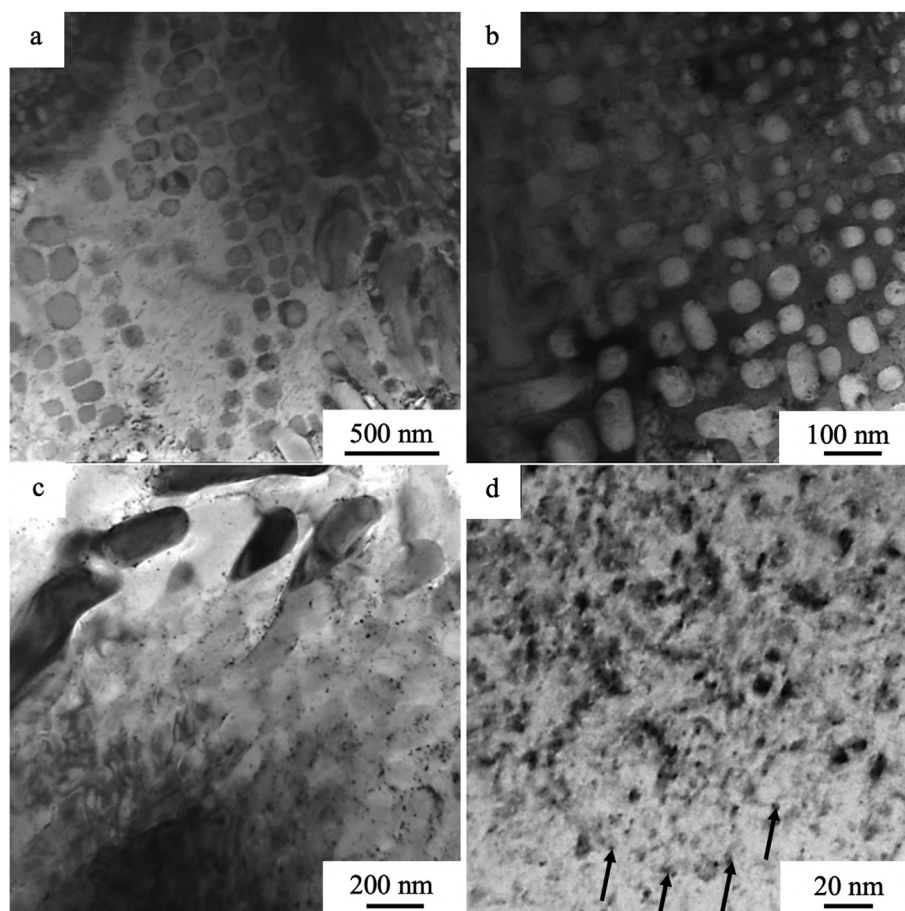


Fig. 5 – Electron microscopic images of the HEA structure obtained when studying thin foils.

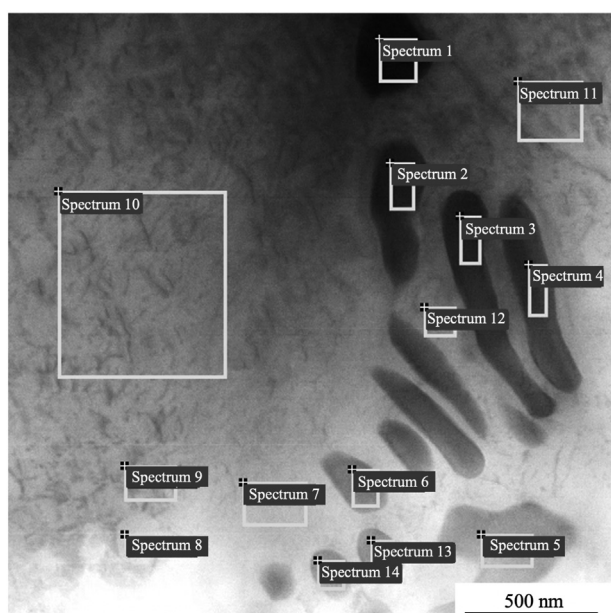


Fig. 6 – STEM image of the HEA foil section. The areas, from which micro-X-ray analysis of the alloy was done, are indicated.

and 10 mm from substrate amounted to 47 ± 5 HRC on average. The obtained hardness is in correlation with the hardness of steel grade 45 (45 HRC).

On the average, nanohardness of the sample under study amounts to 10.4 ± 0.8 GPa independent of distance to the surface. The elastic modulus measured by the nano-indentation method amounts to 304 ± 15 GPa. As a result of performed tests, the HEA wear factor amounts to 1.4×10^{-4} mm³/N·m, and the friction factor is 0.65.

Preliminary analysis of scientific sources showed that the most frequently the tests for HEA plastic properties are carried out by the uniaxial compression method. In this context, a decision was made to perform the main tests by the method of uniaxial compression and the additional tests – by the method of uniaxial tension. To realize the tests by the method of uniaxial compression the cylindrical samples 10 mm in height and 5 mm in diameter were cut out of a HEA bulk sample by electroerosive method. For uniaxial tension tests, the samples 2.3 mm thick \times 9.1 mm wide \times 16.0 mm long (length of working part) were manufactured.

The results of compression tests of HEA samples obtained at different modes of sample formation showed that the ultimate strength of material manufactured by mode No. 1 is in the interval from 652 MPa to 856 MPa, by mode No. 2 it is in the interval from 1361 MPa to 1899 MPa, by mode No. 3 – it is in the interval from 556 MPa to 1390 MPa. The Young's modulus of samples manufactured by the modes has the value of

Table 1 – The results of the quantitative analysis of elemental composition of foil portion in atomic %. Its STEM image is shown in Fig. 7.

Spectrum	C	O	Al	Si	Cr	Fe	Co	Ni
Spectrum 1	46.60	1.07	0.88	0.44	40.38	6.59	1.00	3.05
Spectrum 2	52.95	−0.08	1.02	0.49	35.55	6.09	0.94	3.04
Spectrum 3	50.71	1.60	0.88	0.66	35.29	6.51	0.88	3.49
Spectrum 4	53.50	1.28	1.47	0.45	31.82	6.52	1.01	3.95
Spectrum 5	64.44	3.49	0.85	0.57	19.47	4.89	1.05	5.23
Spectrum 6	63.23	2.53	1.39	0.80	20.82	5.49	1.07	4.67
Spectrum 7	30.80	5.85	9.95	3.03	12.62	19.83	3.88	14.03
Spectrum 8	59.41	5.16	9.61	1.83	2.43	6.12	2.13	13.31
Spectrum 9	37.40	1.55	12.27	2.65	10.50	16.76	3.52	15.35
Spectrum 10	13.03	5.25	7.44	4.27	21.99	30.76	4.92	12.35
Spectrum 11	20.44	2.21	19.99	2.07	10.55	18.65	4.15	21.94
Spectrum 12	37.35	1.21	10.61	3.01	12.87	18.61	3.44	12.90
Spectrum 13	66.20	−0.43	1.57	0.86	19.37	5.46	1.34	5.64
Spectrum 14	63.67	1.91	1.31	0.91	18.94	6.32	1.39	5.56

165–212 GPa (mode No. 1), 273–372 GPa (mode No. 2), 192–270 GPa (mode No. 3). Therefore, the samples manufactured by mode No. 2 possess the largest value of ultimate conditional strength and Young's modulus compared to the samples fabricated by two other modes. It should also be noted that at the failure of samples manufactured by modes No. 1 and No. 3 the jumps on deformation curves were observed. The latter may be caused by the presence of microcracks and micropores in samples manufactured by the modes (No. 1 and No. 3).

The tests for tension at the temperature of 20 °C revealed a brittle failure of obtained samples independent of the place where the samples were cut from a solid massive. The failure occurred by the intergranular cleavage mechanism along the plane at an angle of 45° to the tension axis. Ultimate tensile strength amounted to 4 MPa on average. A source of local failure was a second phase particle located in the junction of four grains. Microrelief of adjacent grains is different that is

indicative of their different crystallographic orientation (Fig. 7).

Fig. 8 represents the HEA surface structure's images in irradiation with pulsed electron beam at a different electron beam's energy density. When analyzing the figures' results, the following features of the structure of irradiation surface being formed may be noted. First of all, we emphasize that the HEA irradiation independent of the energy density of electron beam is accompanied by fragmentation of sample surface by microcracks' network. The fragments sizes reach several hundred micrometres, essentially increasing in grain sizes of the initial alloy. Microcracks form due to relaxations of elastic stresses arising in the material surface layer on velocity cooling taking place in conditions of irradiation by the pulsed electron beam of submillisecond duration effect. The relaxation of elastic stresses by microcrack formation is typical of ceramic materials and indicates increased brittleness of HEA under study.

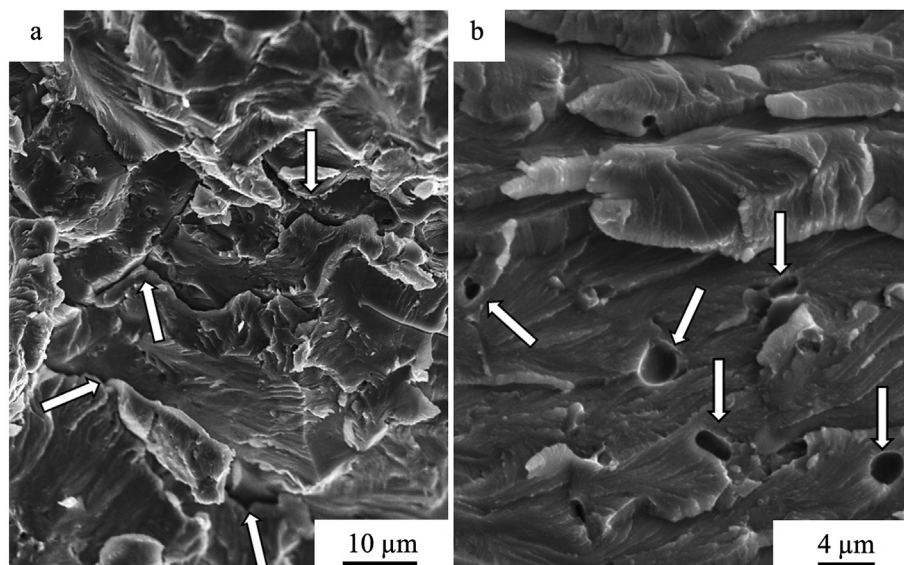


Fig. 7 – Electron microscopic image of typical structural elements of HEA failure surface subjected to uniaxial compression strain. Arrows (a), designate second phase particles being a source of sample local failure. Arrows (b), indicate micropores.

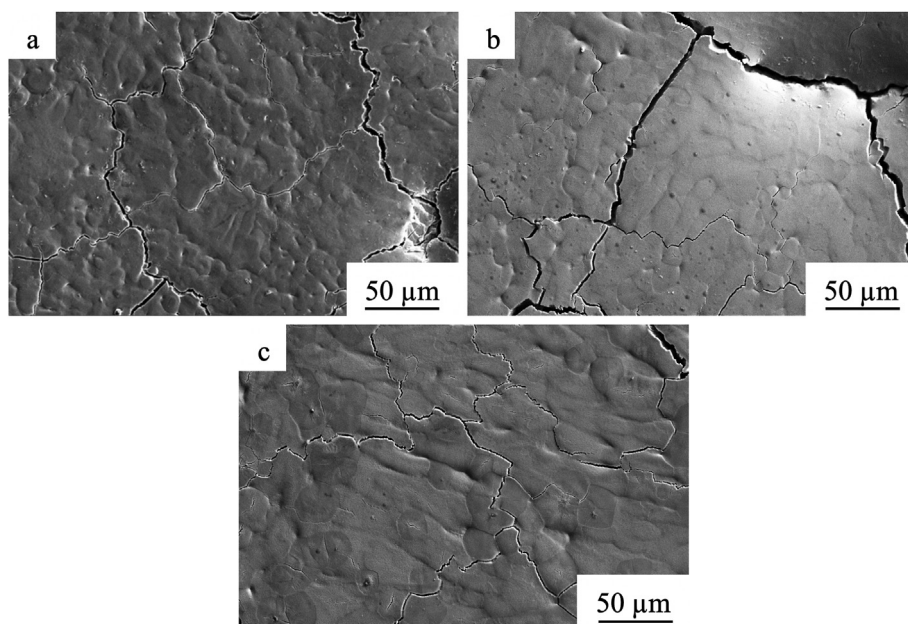


Fig. 8 – SEM image of HEA structure being formed on irradiation by pulsed electron beam ($E_s = 10 \text{ J/cm}^2$ (a), 20 J/cm^2 (b), 30 J/cm^2).

The HEA irradiation by the pulsed electron beam in the mode of surface layer melting is accompanied by material homogenization, as evidenced by the release of grain boundaries from second phase precipitations. The increase in the electron beam's energy density results in the intensification of alloy homogeneous formation processes in elemental composition.

The formation of the submicronanocrystalline structure accompanies high-velocity crystallization of melted surface layer of HEA samples. The sizes of crystallites increase with the growth of energy density of electron beam and vary at $E_s = 30 \text{ J/cm}^2$ in the limits from 100 nm to 200 nm.

There is some probability that alloy irradiation by the pulsed electron beam in the surface layer melting mode may result in an uncontrolled change in the material's elemental composition. The investigations into the elemental composition of the HEA surface layer irradiated by pulsed electron beam carried out by micro-X-ray spectral analysis methods proved no truth of the apprehensions. As it follows from the analysis of results shown in Table 2, the alloy surface layer's elemental composition is practically independent of the electron beam's energy density. It corresponds to the

elemental composition of the initial material within the limits of measurement error.

The scanning electron microscopy methods carried out the investigations into the surface structure of brittle fracture of HEA samples modified by the pulsed electron beam. It is established that the high-velocity crystallization of the surface layer results in the formation of the columnar structure, whose characteristic image is shown in Fig. 9.

The thickness of the modified layer (H) increases from 0.8 μm to 20 μm in a regular way with an increase in energy density of electron beam from 10 J/cm^2 to 30 J/cm^2 (Table 3). The columnar structure is formed by crystallites whose sizes (h) increase regularly with the growth of energy density of the electron beam (Table 3). Thus, such parameter as the energy density of the electron beam affects both the thickness of the modified layer and the size of crystallites being formed due to processing.

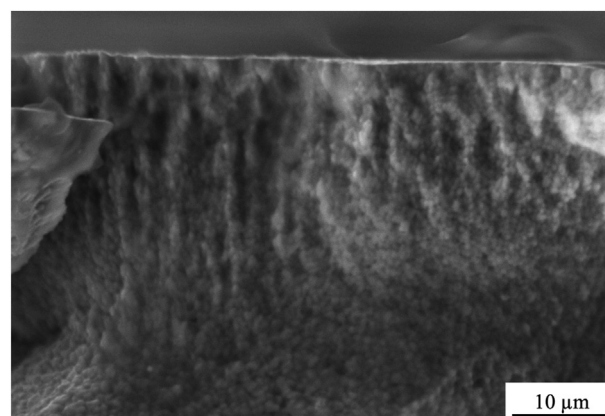


Fig. 9 – SEM image of HEA fracture structure processed by pulsed electron beam with energy density of 30 J/cm^2 .

Table 2 – Results of micro-X-ray spectral analysis of HEA samples in initial state and irradiated by pulsed electron beam at different energy density of electron beam.

$E_s, \text{ J/cm}^2$	Concentration at. %				
	Al	Cr	Fe	Co	Ni
Initial	36.5	8.6	16.4	4.9	33.7
10	33.1	8.8	16.8	5.0	36.3
15	34.4	8.2	16.0	5.0	36.4
20	34.8	7.4	15.3	5.3	37.2
25	34.1	8.3	16.4	5.0	36.2
30	32.8	8.0	16.0	5.3	37.9

Table 3 – Comparative data on layer thickness (H) and surface substructure size (h) depending on energy density of electron beam.

Characteristics of columnar structure	Energy density electron beam, J/cm ²				
	10	15	20	25	30
H, μm	0,8-1	9–10	13	13–15	20
h, μm	Not revealed	0.15–0.3	0.3	1.0	2.5–3.0

The investigations into the elemental composition of samples irradiated by pulsed electron beam are performed using micro-X-ray spectral analysis of transverse metallographic sections. It is found that electron beam processing results in a more homogeneous distribution of elements in the processed layer. So, the enrichment in aluminium and nickel of grain volume being observed in the unprocessed alloy and the enrichment in iron and chromium (Fig. 9) of grain boundaries are not observed in the modified alloy. Mapping of sample cross-section depending on the distance from surface showed that thickness of homogenized layer reaches 4 μm. With the larger increase in distance from the irradiation surface, the distribution of elements characteristic of the unprocessed sample is observed.

By the methods of energy dispersion spectral analysis, it was detected that, on average, the processed layer has the following elemental composition: 39.05 at. % Al, 4.88 at. % Co, 7.92 at. % Cr, 15.9 at. % Fe, 32.25 at. % Ni. The data testify to the increase in aluminium content in the layer and the corresponding decrease in iron, nickel, cobalt and chromium. The

sample irradiation by pulsed electron beam results in no change in material phase composition.

The displacement of HEA diffraction lines to large angles is observed after irradiation, indicating a possible change in the alloy crystal lattice parameter. The results depicted in Fig. 10 show that the alloy crystal lattice parameter after irradiation depends on the energy density of the electron beam in a non-monotonous way and is characterized by essentially smaller value relative to the initial material. Simultaneously, with the

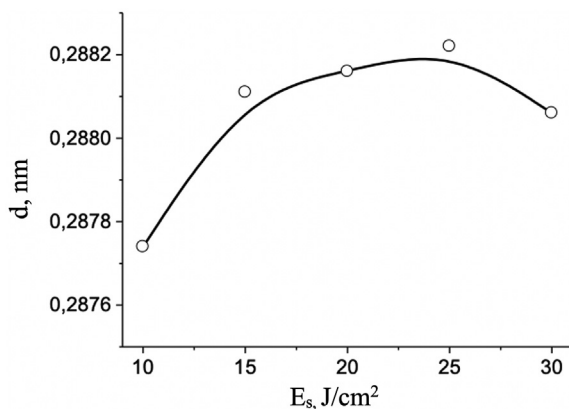


Fig. 10 – A plot of HEA crystal lattice parameter as function of energy density of electron beams. The alloy crystal lattice parameter prior to irradiation (initial state) amounts to 0.28914 nm.

Table 4 – Results of tribological tests.

Energy density of electron beam, J/cm ²	Wear rate, 10 ⁻⁴ mm ³ /N·m	Friction coefficient
Initial sample	1.4	0.65
10	1.9	0.65
15	2.3	0.67
20	1.4	0.63
25	2.5	0.65
30	1.9	0.63

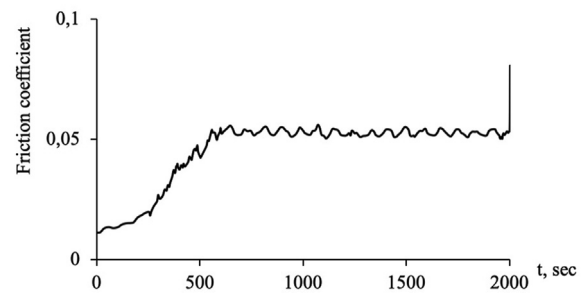


Fig. 11 – Friction coefficient value versus duration of HEA samples tests for wear resistance curve. Lines designate test time at which friction coefficient value is less than 0.2.

Table 5 – Time of HEA-2 sample tests for friction versus energy density of electron beam at which friction coefficient is less than 0.2.

Energy density of electron beam, J/cm ²	0	10	15	20	25	30
Test time, sec (μ = 0,2)	180	240	256	292	143	128

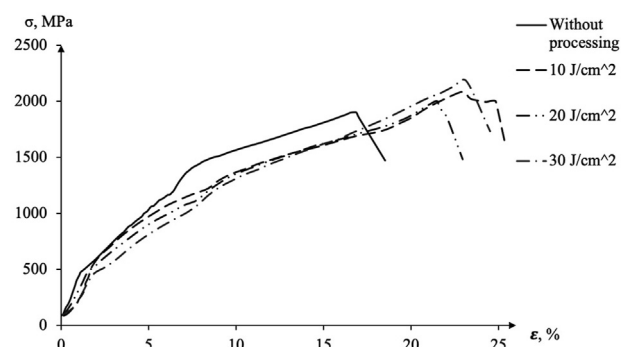


Fig. 12 – Stress–strain diagrams of HEA samples in initial state and processed by electron beams.

Table 6 – Mechanical properties of HEA sample before and after electron beam processing revealed in uniaxial compression tests.

	$\sigma_{0.2}$, MPa	σ_b , MPa	E, GPa	ϵ , %
Initial state	512–523	1361–1899	273–372	9–18
10 J/cm ²	522	2078	310	25
20 J/cm ²	474	2000	279	23
30 J/cm ²	522	2179	257	25

change in crystal lattice parameter, the irradiation leads to decreased microdistortions of the alloy crystal lattice and the increase in sizes of coherent scattering regions.

It is detected that electron beam processing of alloy sample surface at different electron beam densities resulted in the decrease in surface layer microhardness independent of processing parameters. The values decreased on average by 100 HV in the processed layer relative to material bulk. The least microhardness value was observed in processing mode with the energy density of electron beam of 10 J/cm², it amounted to 368 ± 1 HV on the surface. The largest microhardness value of the processed surface of 403 ± 6 HV was detected in the material processed with the energy density of the electron beam of 25 J/cm². It is established that electron beam processing results in a change in surface layer microhardness to the depth up to 90 μm .

The results of investigations into nanohardness and elastic modulus of processed samples revealed a correlation with data on change in microhardness, namely, nanohardness and Young's modulus of surface layer decreased by 28–30% on average. The fact testifies that electron beam processing leads to relaxation of internal stress fields formed in the initial material on its manufacturing.

The performed tribological tests of samples in the initial state and after electron beam processing in different modes showed that electron beam processing affects the friction coefficient and wear rate slightly. The wear rate value of unprocessed sample amounts to $1.4 \times 10^{-4} \text{ mm}^3/\text{N}\cdot\text{m}$, and in samples processed by electron beam, the values vary from 1.4 to $2.5 \times 10^{-4} \text{ mm}^3/\text{N}\cdot\text{m}$. The friction coefficient amounts to 0.65 for initial samples and 0.63–0.67 for modified ones (Table 4).

As a result of tribological tests, the value of the HEA friction coefficient at the initial stage of tests depends substantially on the energy density of the electron beam. The test results presented in Fig. 11 show that at the initial stage of tests (up to 300 s), the friction coefficient of irradiated samples is less than 0.2. On increasing the test time, the friction coefficient increases and comes to a plateau corresponding to the friction coefficient value of the initial material ($\mu = 0.7$). It may be suggested that the change in friction coefficient is related to

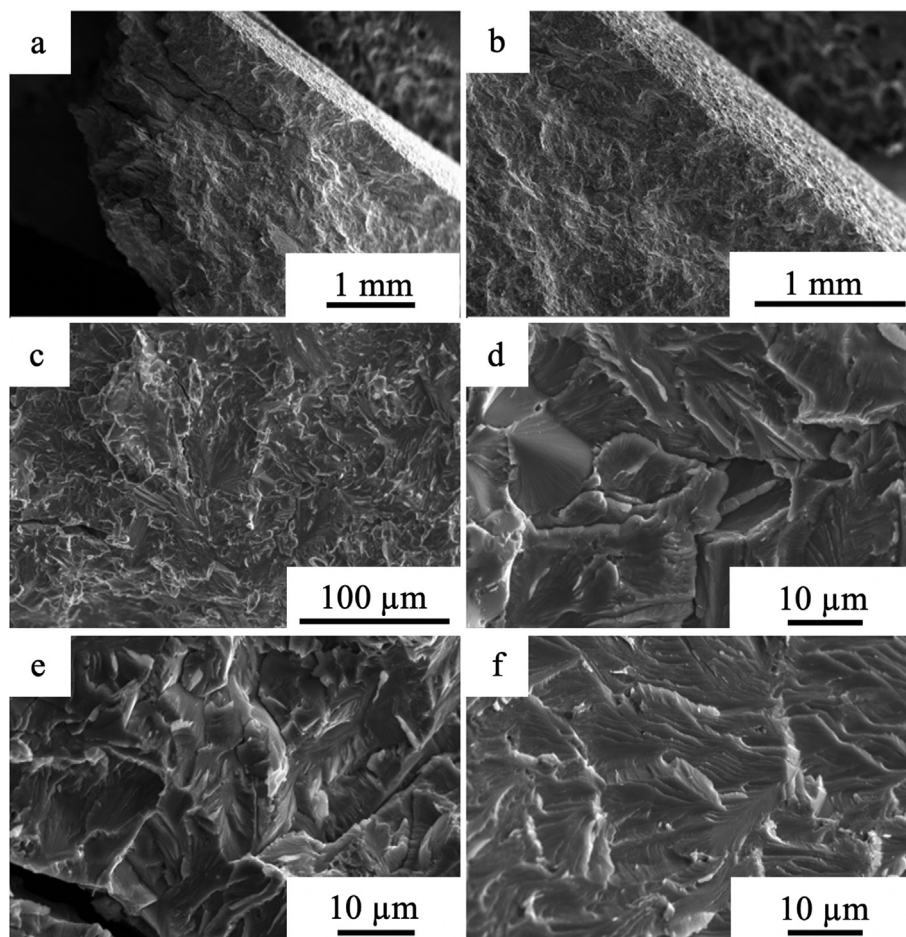


Fig. 13 – Structure of failure surface being formed in HEA sample compression. Scanning electron microscopy. a-f indicate different magnification.

two moments. First, the presence of a modified layer after irradiation whose friction coefficient is small; second, the failure of the layer and participation of base material in wear.

If we take $\mu = 0.2$ as a benchmark, then it turns out that the friction coefficient depends nonmonotonously on the energy density of the electron beam in this test time interval. The best tribological properties are shown by the sample irradiated at an energy density of electron beam of 20 J/cm^2 , for which time interval reaches 300 s (Table 5).

Irradiation of high-entropy alloy by intense pulsed electron beam led to an increase in the material's strength and plasticity. So, ultimate compression strength increased by 1.1–1.6 times (Fig. 12). The largest ultimate compression strength value of 2179 MPa was obtained in the alloy processed by an electron beam with an energy density of 30 J/cm^2 . The conditional ultimate compression strength, in this case, amounted to 522 MPa, and Young's modulus amounted to 257 GPa (Table 6).

A characteristic image of the surface being formed in HEA failure conditions of compression is shown in Fig. 13. The investigations carried out revealed a failure structure similar to that being formed in HEA sample failure in uniaxial tension conditions (see Fig. 8). Namely, in the bulk of grains, a grooved pattern is present that is steps between different local cleavage facets of the same common plane. The source of local failure is particles of the second phase located in the junction of grains.

4. Conclusions

By means of wire-arc additive manufacturing technology, the samples of high-entropy alloy AlCoCrFeNi of the following elemental composition (at. %): 28.40 Al, 6.47 Co, 8.36 Cr, 19.57 Fe, 37.20 Ni have been fabricated. The irradiation of the HEA sample surface by the pulsed electron beam in the surface layer melting mode has been carried out.

The following major conclusions were drawn from the present study:

1. The as-manufactured samples have a brittle structure with high microhardness (465–474 HV). Compression tests showed that the samples' ultimate strength lies in the range from 556 MPa to 1899 MPa for different regimes.
2. X-ray diffraction analysis showed that the material has a primitive cubic structure with a lattice constant of 0.288337 nm and a space group of Pm3m.
3. Irradiation by electron beams increases the ultimate compression strength by 1.1–1.6 times. The largest value of ultimate compression strength of 2179 MPa was obtained in the alloy processed by an electron beam with an energy density of 30 J/cm^2 .
4. HEA irradiation by the pulsed electron beam is accompanied by the release of grain boundaries from the second phase precipitations that indicates the material homogenization. The phase composition of the alloy was not changed.
5. It is established that electron beam processing decreases the surface layer microhardness by about 65–100 HV to a depth up to 90 μm .

6. Tribological tests revealed that as-manufactured HEA wear coefficient amounted to $1.4 \times 10^{-4} \text{ mm}^3/\text{N}\cdot\text{m}$ and friction coefficient amounted to 0.65. Simultaneously, irradiation of high-entropy alloy by intense pulsed electron beam affected the friction coefficient and slightly affected material wear rate.

Declaration of Competing Interest

The authors declare that they have no known competing financial interests or personal relationships that could have appeared to influence the work reported in this paper.

Acknowledgments

The research was supported by Russian Science Foundation grant (project No 20-19-00452).

REFERENCES

- [1] Tong C-J, Chen Y-L, Yeh J-W, Lin S-J, Lee P-H, Shun T-T, et al. Microstructure characterization of Al_xCoCrCuFeNi high-entropy alloy system with multiprincipal elements. *Metall Mater Trans* 2005;36:881–93. <https://doi.org/10.1007/s11661-005-0283-0>.
- [2] Chen YY, Duval T, Hung UD, Yeh JW, Shih HC. Microstructure and electrochemical properties of high entropy alloys—a comparison with type-304 stainless steel. *Corrosion Sci* 2005;47:2257–79. <https://doi.org/10.1016/j.corsci.2004.11.008>.
- [3] Pradeep KG, Wanderka N, Choi P, Banhart J, Murty BS, Raabe D. Atomic-scale compositional characterization of a nanocrystalline AlCrCuFeNiZn high-entropy alloy using atom probe tomography. *Acta Mater* 2013;61:4696–706. <https://doi.org/10.1016/j.actamat.2013.04.059>.
- [4] Daoud HM, Manzoni A, Völkl R, Wanderka N, Glatzel U. Microstructure and tensile behavior of Al₈Co₁₇Cr₁₇Cu₈Fe₁₇Ni₃₃ (at.%) high-entropy alloy. *J Occup Med* 2013;65:1805–14. <https://doi.org/10.1007/s11837-013-0756-3>.
- [5] Lin C-M, Tsai H-L. Evolution of microstructure, hardness, and corrosion properties of high-entropy Al_{0.5}CoCrFeNi alloy. *Intermetallics* 2011;19:288–94. <https://doi.org/10.1016/j.intermet.2010.10.008>.
- [6] Tariq NH, Naeem M, Hasan BA, Akhter JI, Siddique M. Effect of W and Zr on structural, thermal and magnetic properties of AlCoCrCuFeNi high entropy alloy. *J Alloys Compd* 2013;556:79–85. <https://doi.org/10.1016/j.jallcom.2012.12.095>.
- [7] Hsu Y-J, Chiang W-C, Wu J-K. Corrosion behavior of FeCoNiCrCu high-entropy alloys in 3.5% sodium chloride solution. *Mater Chem Phys* 2005;92:112–7. <https://doi.org/10.1016/j.matchemphys.2005.01.001>.
- [8] Chen M-R, Lin S-J, Yeh J-W, Chuang M-H, Lee P-H, Huang Y-S. Effect of vanadium addition on the microstructure, hardness, and wear resistance of Al_{0.5}CoCrCuFeNi high-entropy alloy. *Metall Mater Trans A-Physical Metall Mater Sci - Met MATER TRANS A* 2006;37:1363–9. <https://doi.org/10.1007/s11661-006-0081-3>.
- [9] Hsu US, Hung UD, Yeh JW, Chen SK, Huang YS, Yang CC. Alloying behavior of iron, gold and silver in AlCoCrCuNi-

- based equimolar high-entropy alloys. *Mater Sci Eng, A* 2007;460–461:403–8. <https://doi.org/10.1016/j.msea.2007.01.122>.
- [10] Chen M-R, Lin S-J, Yeh J-W, Chen S-K, Huang Y-S, Tu C-P. Microstructure and properties of Al_{0.5}CoCrCuFeNiTi_x (x=0–2.0) high-entropy alloys. *Mater Trans* 2006;47:1395–401. <https://doi.org/10.2320/matertrans.47.1395>.
- [11] Dolique V, Thomann A-L, Braut P, Tessier Y, Gillon P. Thermal stability of AlCoCrCuFeNi high entropy alloy thin films studied by in-situ XRD analysis. *Surf Coating Technol* 2010;204:1989–92. <https://doi.org/10.1016/j.surfcoat.2009.12.006>.
- [12] Li B, Peng K, Hu A, Zhou L, Zhu J, Li D. Structure and properties of FeCoNiCrCu_{0.5}Al_x high-entropy alloy. *Trans Nonferrous Met Soc China* 2013;23:735–41. [https://doi.org/10.1016/S1003-6326\(13\)62523-6](https://doi.org/10.1016/S1003-6326(13)62523-6).
- [13] Qiu X-W. Microstructure and properties of AlCrFeNiCoCu high entropy alloy prepared by powder metallurgy. *J Alloys Compd* 2013;555:246–9. <https://doi.org/10.1016/j.jallcom.2012.12.071>.
- [14] Liu L, Zhu JB, Zhang C, Li JC, Jiang Q. Microstructure and the properties of FeCoCuNiSn_x high entropy alloys. *Mater Sci Eng, A* 2012;548:64–8. <https://doi.org/10.1016/j.msea.2012.03.080>.
- [15] Singh S, Wanderka N, Murty BS, Glatzel U, Banhart J. Decomposition in multi-component AlCoCrCuFeNi high-entropy alloy. *Acta Mater* 2011;59:182–90. <https://doi.org/10.1016/j.actamat.2010.09.023>.
- [16] Stepanov ND, Shaysultanov DG, Chernichenko RS, Yurchenko NY, Zhrebtsov SV, Tikhonovsky MA, et al. Effect of thermomechanical processing on microstructure and mechanical properties of the carbon-containing CoCrFeNiMn high entropy alloy. *J Alloys Compd* 2017;693:394–405. <https://doi.org/10.1016/j.jallcom.2016.09.208>.
- [17] Shun T-T, Du Y-C. Age hardening of the Al_{0.3}CoCrFeNiCo_{0.1} high entropy alloy. *J Alloys Compd* 2009;478:269–72. <https://doi.org/10.1016/j.jallcom.2008.12.014>.
- [18] Kao Y-F, Chen T-J, Chen S-K, Yeh J-W. Microstructure and mechanical property of as-cast, -homogenized, and -deformed Al_xCoCrFeNi (0≤x≤2) high-entropy alloys. *J Alloys Compd* 2009;488:57–64. <https://doi.org/10.1016/j.jallcom.2009.08.090>.
- [19] Otto F, Dlouhý A, Somsen C, Bei H, Eggeler G, George EP. The influences of temperature and microstructure on the tensile properties of a CoCrFeMnNi high-entropy alloy. *Acta Mater* 2013;61:5743–55. <https://doi.org/10.1016/j.actamat.2013.06.018>.
- [20] Gludovatz B, Hohenwarter A, Catoor D, Chang EHEH, George EPEP, Ritchie RORO. A fracture-resistant high-entropy alloy for cryogenic applications. *Science* 2014;345:1153–8. <https://doi.org/10.1126/science.1254581> (80-).
- [21] Cantor B. Multicomponent and high entropy alloys. *Entropy* 2014;16:4749–68. <https://doi.org/10.3390/e16094749>.
- [22] Miracle DB, Senkov ON. A critical review of high entropy alloys and related concepts. *Acta Mater* 2017;122:448–511. <https://doi.org/10.1016/j.actamat.2016.08.081>.
- [23] Zhang W, Liaw PK, Zhang Y. Science and technology in high-entropy alloys. *Sci China Mater* 2018;61:2–22. <https://doi.org/10.1007/s40843-017-9195-8>.
- [24] Pogrebnjak AD, Yakushchenko IV, Bondar OV, Bagdasaryan AA, Beresnev VM, Kolesnikov DA, et al. Influence of the structure and elemental composition on the physical and mechanical properties of (TiZrHfVNB)_N nanostructured coatings. 2015. p. 173–83. <https://doi.org/10.1002/9781119040354.ch19>.
- [25] Pogrebnjak AD, Bondar OV, Yakushchenko IV, Kozak C, Czarnacka K. Influence OF high-dose ION implantation ON the structure and properties OF the nitrides OF high-entropy alloys. *High Temp Mater Process An Int Q High-Technology Plasma Process* 2015;19:257–64. <https://doi.org/10.1615/HighTempMatProc.2016016169>.
- [26] George EP, Curtin WA, Tasan CC. High entropy alloys: a focused review of mechanical properties and deformation mechanisms. *Acta Mater* 2020;188:435–74. <https://doi.org/10.1016/j.actamat.2019.12.015>.
- [27] Rogachev AS. Structure, stability, and properties of high-entropy alloys. *Phys Met Metallogr* 2020;121:733–64. <https://doi.org/10.1134/S0031918X20080098>.
- [28] Zhang C, Lv P, Xia H, Yang Z, Konovalov S, Chen X, et al. The microstructure and properties of nanostructured Cr-Al alloying layer fabricated by high-current pulsed electron beam. *Vacuum* 2019;167:263–70. <https://doi.org/10.1016/j.vacuum.2019.06.022>.
- [29] Ivanov YF, Gromov VE, Konovalov SV, Zagulyaev DV, Petrikova EA, Semin AP. Modification of structure and surface properties of hypoeutectic silumin by intense pulse electron beams. *Usp Fiz Met* 2018;19:195–222. <https://doi.org/10.15407/ufm.19.02.195>.
- [30] Ivanov YF, Gromov VE, Konovalov SV. Electron-beam modification of the pearlite steel. *Arabian J Sci Eng* 2009;34:233–43. <https://doi.org/10.1111/J.2191.4281>.
- [31] Liu Y, Zhang K, Zou J, Yan P, Zhang X, Song L. Microstructure and property modifications in surface layers of a Mg-4Sm-2Al-0.5Mn alloy induced by pulsed electron beam treatments. *J Magnes Alloy* 2021;9:216–24. <https://doi.org/10.1016/j.jma.2020.02.019>.
- [32] Panin SV, Vlasov IV, Sergeev VP, Maruschak PO, Sunder R, Ovechkin BB. Fatigue life improvement of 12Cr1MoV steel by irradiation with Zr⁺ ion beam. *Int J Fatig* 2015;76:3–10. <https://doi.org/10.1016/j.ijfatigue.2014.10.011>.
- [33] Safdar A, He HZ, Wei L, Snis A, Chavez de Paz LE. Effect of process parameters settings and thickness on surface roughness of EBM produced Ti-6Al-4V. *Rapid Prototyp J* 2012;18:401–8. <https://doi.org/10.1108/13552541211250391>.
- [34] Proskurovsky DI, Rotshtein VP, Ozur GE, Markov AB, Nazarov DS, Shulov VA, et al. Pulsed electron-beam technology for surface modification of metallic materials. *J Vac Sci Technol A Vacuum, Surfaces, Film* 1998;16:2480–8. <https://doi.org/10.1116/1.581369>.